RSC Advances

ROYAL SOCIETY OF CHEMISTRY

www.rsc.org/advances

Bubble template synthesis of $CdLa_2S_4$ hollow spheres/reduced graphene oxide nanocomposites as efficient and sustainable visible-light driven photocatalysts

Lei Zhu, and Won-Chun Oh*

Department of Advanced Materials Science & Engineering, Hanseo University, Seosan-si, Chungnam-do, Korea, 31962

A hollow sphere $CdLa_2S_4$/reduced graphene oxide (rGO) composite was successfully synthesized for the first time via a simple microwave assisted hydrothermal approach using bubbles generated from the decomposition of NH_3H_2O and $Na_2S_2O_3$ in a domestic microwave oven within several minutes. The large number of catalytic active sites together with the advantages of the hollow structure makes the as-synthesized $CdLa_2S_4$/rGO composite an efficient catalyst for the degradation of rhodamine B (Rh.B) and industrial dyes such as Texbrite BA-L (TBA) with high concentration in aqueous solutions. The oxidation reaction of 1,5-diphenyl carbazide (DPCI) by a generated reactive oxygen species (ROS) that has very strong oxidability could be attributed to the excellent photoinduced charge separation abilities and observed red shift in these hybrid semiconductor materials. Moreover, the synthesized catalyst can be easily recovered and reused for at least four cycles due to its good stability. The results confirm that as-synthesized $CdLa_2S_4$/rGO composites are promising potential candidates for high-performance visible light driven photocatalyst materials.

Keywords: $CdLa_2S_4$, Graphene oxide, Hollow nanosphere, Microwave synthesis, Visible light

*Corresponding author.
E-mail: wc_oh@hanseo.ac.kr
Tel: +82-41-660-1337, Fax:+82-41-688-3352

Introduction

Hollow-structured materials hollow inorganic spheres with low densities, high surface areas, and unique electronic, magnetic, and chemical properties have become an interesting topic for research. The spheres have promising applications in photonic catalysts,[1] drug-delivery carriers,[2] electronic devices,[3] controlled release,[4] and optical sensors for high-power laser irradiation.[5] In order to prepare hollow structures, soft templates such as surfactants,[6] liquid crystal template,[7,8] micelles,[9] or gas bubbles,[10-12] have been commonly used due to it is simple and inexpensive.

Graphene is a new star on applications of condensed-matter physics, electronics, and material science after carbon nanotube and C_{60}.[13] Graphene is a single-atom thick sheet arranged by sp2-bonded carbon atoms in a hexagonal lattice, which shows outstanding mechanical, thermal, optical, and electrical properties. Therefore, the interesting graphene-based hollow-structured materials have been extremely extended to application. Huang et al. synthesize the rGO wrapped hollow CuS sphere composite by in situformation of hollow CuS sphere on the surface of rGO nanosheet under simple one-step solvothermal route assisted by ethylene glycol as electrode material for supercapacitor.[14] Mi et al. reported for the first time CdS hollow spheres supported on the surface of N-graphene nanosheets (N-graphene/CdS HSNs), and present a simple, template-free one-pot method for their fabrication.[15] The prepared samples were found to exhibit higher photocatalytic activity than that of graphene oxide (GO)/CdS HSNs and sole CdS hollow spheres during photocatalytic degradation experiments. Ou et al. reported droplet-shape hollow Ni_3S_2 nanoparticles, as well as corresponding partially nickel-filled nanoparticles, of narrow diameter distribution and uniform dispersion were successfully synthesized on two-dimensional graphene templates using a facile process with moderate reaction conditions.[16]

As a common semiconductor material, transition-metal chalcogenides have attracted much attention due to their excellent properties and wide-ranging potential applications.[17,18] $CdLa_2S_4$, as a ternary semiconductor chalcogenide has a strong absorption in the visible light region with band gap energy of 2.1ev, therefore it has become a good catalyst for photo-degradation of organic pollutants and photoproduction of hydrogen from water in the past few

years.[19,20] Kale et al. reported synthesis of self-assembled $CdLa_2S_4$ hexagon flowers, nanoprisms and nanowires via a facile hydrothermal method at 433K, followed application in H_2 production in water/methanol solution.[19] Hou et al. found that the coupling of CdS nanoparticles with $CdLa_2S_4$ microspheres via a two-step hydrothermal process led to significant increase in the photocatalytic H_2 production rate, nevertheless Pt-loading was still required for H_2 evolution.[21] However, to our knowledge, there is still a need to develop a more straight forward procedure for fabricating graphene based hollow structured $CdLa_2S_4$ in an effective and reproducible fashion and applications on photo-degradation of organic pollutants.

It is well known that the synthesis of nanomaterials with uniform size, shape and high crystallinity is one of the important challenging problems. There are various kinds of synthesis methods available for the preparation of nanomaterials such as hydrothermal, microwave synthesis, sol–gel, micro emulsion and the polyol technique. As compared to common methods, the microwave synthesis technique provides such advantages as a very short reaction time, small particle size, narrow particle size distribution and it is the high purity method suitable for the preparation of polycrystalline products.[22] The microwave heating is delivered to the surface of the material by radiant and/or convection heating, which is transferred to the bulk of the material via conduction. So, the microwave energy is delivered directly to the material through the molecular interactions with electromagnetic field. Heat can be generated through volumetric heating because microwaves can penetrate the material and supply energy.[23]

Herein, this is the first report for the synthesis of graphene nanosheets coated with $CdLa_2S_4$ nanometer-sized hollow spheres obtained directly via a facile microwave assisted synthesis method[24] in a domestic microwave oven without using a surfactant. To clarify the possible formation mechanism of $CdLa_2S_4$ hollow spheres on the graphene nanosheet, the microwave assisted synthesis reaction time has been investigated. The as-synthesized $CdLa_2S_4$/rGO nanocomposite show highly enhanced photocatalytic performance for degradation of different organic dyes, rhodamine B (Rh.B) and Texbrite BA-L (TBA), with high concentration in aqueous solutions under visible light irradiation, due to the existence of

the strong interaction between $CdLa_2S_4$ hollow spheres and rGO.

Experimental

Materials

Ethylene glycol and anhydrous ethanol were purchased from Daejung Chemical Co. (Korea). Sulfuric acid (H_2SO_4), potassium permanganate ($KMnO_4$), H_2O_2 and $(CH_3COO)_2Cd{\cdot}2H_2O$, $La(NO_3)_3{\cdot}H_2O$, $Na_2S_2O_3$ were supplied by Daejung Chemical Co., Ltd, Korea. Texbrite BA-L was purchased from Texchem Co. Ltd, Korea. Rh.B ($C_{28}H_{31}ClN_2O_3$, 99.99+%) was used as the model pollutant and was purchased from Samchun Pure Chemical Co., Ltd, Korea. Ammonium hydroxide (NH_3H_2O) was purchased from Duksan Pure Chemical Co. (Korea) and used as received. All chemicals were used without further purification and all experiments were carried out using distilled water.

Synthesis of $CdLa_2S_4$/rGO nanocomposites

In a typical experiment, about 20mg Graphite oxide (GO) prepared from graphite according to the Hummers-Offeman method in our early reports[25] was dispersed in 80ml ethylene glycol and then exfoliated to generate graphene oxide nanosheets (GONS) dispersion solution by ultrasonication for 25min using a digital sonifer.[26] Subsequently, calculated amount of $(CH_3COO)_2Cd.2H_2O$ and $La(NO_3)_3.H_2O$ were added to the GONS aqueous dispersion, followed by ultrasonication for 20min. Afterwards, sodium thiosulfate anhydrous ($Na_2S_2O_3$) and 5mL ammonium hydroxide (NH_3H_2O) were added to the mixture transferred into a 120 mL reaction vessel and placed in a conventional microwave oven (Samsung, RE-406B 700 W). The solution is then irradiated by microwave at full power for 10 sec on and 10 sec off for 5min, and cooled at room temperature washed several time with hot water and transferred into a dry oven. The ammonia promised it to obtain maximal charge so as to prevent the aggregation of graphene oxide caused by salt effect,[27] which was in favor of the uniform distribution of $CdLa_2S_4$ on GONS. The $Na_2S_2O_3$ was taken as 0.5, 0.75 and 1mM and the final product labeled as CdG1, CdG2, CdG3 were rinsed with distilled water and ethanol for several times, and dried at 60 °C for 12 h. Bulk $CdLa_2S_4$ nanoparticle was also synthesized by the same procedure except that no GONS was used. The preparation conditions and schemiatic illustration are shown in Fig.1a.

Characterization

The crystal structures and phases of the samples were obtained by XRD (Shimata XD-D1, Japan) with Cu Kα radiation (λ=1.54056 Å) in the range of 2θ from 10-80^{o} at a scan speed of 1.2^{o} m^{-1}. The morphology of the samples was studied by SEM (JSM-5200 JOEL, Japan). Energy dispersive X-ray spectroscopy (EDX) was also employed for elemental analysis. Transmission electron microscopy (TEM, JEOL, JEM-2010, Japan) was used to observe the surface state and structure of the photocatalyst composites at an acceleration voltage of 200 kV. TEM was also used to examine the size and distribution of the $CdLa_2S_4$ nanoparticles on graphene sheet. Diffuse reflectance spectra were obtained by using a scan UV/Vis spectrophotometer (Neosys-2000) equipped with an integrating sphere assembly. Raman spectra of the samples were observed using a spectrometer (Jasco Model Name NRS-3100) having an excitation laser wavelength of 532.06 nm. FT-IR spectroscopy (FTS 3000MX, Biored Co. Korea) was used to characterize the functional groups of GO and CdG2. The BET surface areas of the photocatalysts were determined by measuring nitrogen adsorption at 77 K using a BET analyzer (Monosorb, USA). The decomposition kinetics for the photocatalytic activity was measured by using spectrometer (Optizen POP, Mecasys, Korea).

Photocatalytic reactions

The photocatalytic activities of the pure $CdLa_2S_4$, CdG1, CdG2, and CdG3 nanocomposites were evaluated from the degradation of Rh.B solution under irradiation of visible light (8W, Fawoo, Lumidas-H, Korea, λ>420 nm). In an ordinary photocatalytic test performed at room temperature, 0.03 g photocatalyst was added to 50 mL of 3.0×10^{-5} mol/L Rh.B solution, which was hereafter considered as the initial concentration (c_0). To achieve more degradation activity of the CdG2 nanocomposite industrial dye, TBA was also conducted with the same conditions. The mixture was sonicated for 10 min and stirred for 120 min in the dark in order to reach adsorption–desorption equilibrium. The first sample was extracted immediately before the light was turned on in order to determine the dye concentration in solution after dark adsorption, which was henceforth considered as the initial concentration (c_{ads}). The samples were then withdrawn regularly from the reactor in the order of 30 min, 60 min, 90 min, 120 min, and 150 min, immediately centrifuged to separate any suspended solid. The

clean transparent solution was analyzed using a UV-vis spectrophotometer (Optizen POP) at a wavelength from 250 nm to 800 nm.

Evaluation of Reactive Oxygen Species (ROS)

In order to detect the type of ROS generated during photocatalytic reactions, the experiments were performed according to a previous reported method.[23] Firstly, four 100 mL transparent volumetric flasks were marked notations (a–d), respectively. Four 10.00 mL DPCI stock solutions (1.00 x 10^{-2} mol/L) were added to a–d correspondingly followed by the addition of a 50 mg sample in the order of (1,2,3,4) from a to d. All four solutions were diluted to 100 mL with double distilled water. The final DPCI concentration and CdG2 amount were 1.00×10^{-3} mol/L and 1.00 g/L, respectively. After 120 min of irradiation, 10 ml of solution was taken from each reactor and extracted with benzene. In the second step, all the extracted solutions were diluted to 10 mL with benzene solution and their UV-Vis spetra were recorded by using a spectrometer.

Results and discussion

Characterization

Fig. 1a shows the deposition of $CdLa_2S_4$ on the GONS. In this approach, Cd^{2+}/La^{3+} were captured by hydroxyls (possible epoxies or carboxyls) on the GO by coordination. The Cd^{2+}/La^{3+} ions in situ then reacted with S^{2-} under hydrothermal treatment to form $CdLa_2S_4$ nanoparticles with the simultaneous reduction of the graphene oxide (GO). Fig. 1b shows the XRD pattern of the product obtained from the above procedure. It can be seen that the diffractogram of graphene exhibits typical peaks at 25.9° and 42.7°, corresponding to the graphite (002) and (100) reflections (Joint Committee for Powder Diffraction Studies (JCPDS) No. 01-0646), [26] respectively. In the $CdLa_2S_4$ and $CdLa_2S_4$/rGO composites all the diffraction peaks around at 2θ of 18.07°, 26.8°, 43.8°, and 51.9° could be indexed to $CdLa_2S_4$, indicating that single phase $CdLa_2S_4$ was obtained. This result is consistent with those of the previous report. [19] However, no signal for any other phases of GO (001) or graphene (002) could be detected in GR-$CdLa_2S_4$ composite. According to Ref. [19] GO can be reduced to graphene during the hydrothermal reaction and the synthesized graphene sheets can restack to form poorly ordered graphite along the stacking direction. Earlier studies have shown that if

the regular stack of GO or graphite is broken, such as by exfoliation, their diffraction peaks may also become weak or even disappear.[27]

Further evidence of the deoxygenation of GO to graphene using FT-IR analysis is shown in Fig. 1c. It is well known that some carbon double bonds are oxidized after the acidic intercalation and thermal treatment, resulting in the presence of oxygen-containing functional groups such as -COOH and -OH on the surface of the graphite oxide nanosheets.[28,29] For GO, the resonance at 1619 cm^{-1} can be assigned to the vibrations of the adsorbed water molecules: the C=O carbonyl stretching near 1728 cm^{-1}, the C-OH stretching near 1226 cm^{-1}, and the C-O stretching near 1050 cm^{-1}.

Meanwhile, the amount and distribution of the carboxylic groups have great influence on the further positive-selective modification of graphene sheets with nanoparticles. The positive metal ions in the system would attach to and interact with the carboxylic groups via electrostatic attraction and serve as nucleation precursors.[30] Peaks for C = O functional groups were observed at approximately 1728 cm^{-1}. Comparison of the spectra reveals lower peak intensity for functional groups in oxidized graphene. This is because some of the functional groups combined with $CdLa_2S_4$ particles and removed in the process of reduction of graphene oxide to graphene.[13]

The Raman spectra of GO and CdG2 nanocomposite in Fig. 1d displays the presence of D and G bands at 1350 and 1597 cm^{-1}, respectively. G band is common to all sp^2 carbon forms[31] and provides information on the in-plane vibration of sp^2 bonded carbon atoms.[32] The D band suggests the presence of sp^3 defects.[33] The second-order Raman feature, namely the 2D band (second-order of the D band) at about 2720 cm^{-1} and D+G band at about 2930 cm^{-1} is very sensitive to the stacking order of the graphene sheets along the c-axis as well as to the number of layers, and shows greater structure (often a doublet) with increasing number of graphene layers.[34] Simultaneously, relative intensity of D/G (1.13) was increased compared to that in GO (1.07).[35] This further confirmed that GO was reduced to graphene and indicate the considerable decrease in size of the in-plane sp^2 domains and and a partially ordered crystal structure of the $CdLa_2S_4$/rGO (CdG2) nanocomposites.[36]

The morphologies of $CdLa_2S_4$, graphene, and $CdLa_2S_4$/rGO (CdG2) nanocomposites were investigated using SEM. From Fig. 2a, the overall structure can be clearly predicted,

showing that graphene is a plate-like structure broken off in different direction. A flake-like morphology was observed for graphene, reflecting its layered microstructure. The large interlayer spaces and thin layer edges of graphene can be clearly observed. Fig. 2b shows pure $CdLa_2S_4$ particles appearing as spherical particles with good dispersion and large size. The morphology of the $CdLa_2S_4$/rGO composites substantially differs from that of the graphene sheets. Meanwhile, the spherical $CdLa_2S_4$ nanoparticles with smaller size compared with pure $CdLa_2S_4$ can be observed, showing they were distributed tightly and evenly on the graphene sheets and formed a graphene-based nanostructure composite. Because of the presence of oxygen functionalities on the surface of the graphene sheets, electrostatic force arises among the nanosheet in the form of van der Waals interaction that tends to force the graphene sheet to aggregate back to a graphitic structure. The attachment of nanoparticles on the graphene sheet is helpful to overcome these interactions.[37] The graphene sheet acts as a support material to the $CdLa_2S_4$ particle, which may be advantageous for supplying a path for the generated electron, and will thus improve the photocatalytic behavior of the nanocomposites.

To obtain information about the changes in the elements and element weight %, the prepared $CdLa_2S_4$/rGO composites were examined using EDX. Fig. 2d shows the EDX microanalysis and element weight % of the $CdLa_2S_4$/rGO nanocomposite. The main elements such as C, Cd, La, and S are present. The strong C signal should mainly originate from the graphene nanosheets. The $L\alpha_1$ and $L_{\beta1}$ peaks from the La element appear at 4.65 and 5.04 KeV, respectively, while the S peak originating from the precursor materials of $Na_2S_2O_3$ appears at $K\alpha_1$ 2.309 KeV.

Typical TEM images of graphene, pure $CdLa_2S_4$, and $CdLa_2S_4$/rGO (CdG2) are shown in Fig. 3. The morphology of graphene, consisting of thin stacked flakes with a well-defined fewlayer structure at the edge, is clearly shown in Fig. 3a. Fig. 3b shows a TEM image of pure $CdLa_2S_4$ synthesized via microwave assisted hydrothermal method, which reveal spherical structure and defined single crystal of $CdLa_2S_4$ with a size of 20-25nm. In addition, the $CdLa_2S_4$/rGO (CdG2) nanocomposites with different magnifications are clearly shown in Figs. 3c-3f. The TEM micrograph in Fig. 3c and 3d confirms the formation of hollow nanospheres, where the distinguished contrasts can be found between the outer shells and the inner hollow cores. It was found that most hollow nanospheres are composed of a number of

smaller particles with the size of 15-20nm. The HRTEM image (Figs. 3e and 3f) suggests that the fine $CdLa_2S_4$ particles are single-crystalline. The spacing of the observed lattice fringe is identified as 0.36 nm, which is associated with the {211} plane of the cubic phase $CdLa_2S_4$.[20]

The quest for the design of new photocatalyst materials that utilize the entire energy spectrum is very important. For the purification or removal of environmental pollutants, an ideal photocatalyst must have maximum efficiency in both the UV and visible range of the electromagnetic spectrum. The UV-vis absorption spectra of the different samples are presented in Fig. 4a. Due to the carbonated structure of graphene, the unpaired π electron may cause an interaction with the metal nanoparticles. Such reduction may cause a shift in the band edges and increase the light absorption towards the visible region region.[38] Lee et al also observed such kind of effect with titanium nanoparticles and observed the optical response towards the visible region of electromagnetic spectrum.[39] It can be clearly seen that $CdLa_2S_4$ and $CdLa_2S_4$/rGO (CdG1, CdG2, CdG3) composites have great absorption in the ultraviolet region. Moreover, for the CdG1, CdG2, and CdG3 composites, the absorption intensities are significantly increased in the entire visible region, confirming the effectively improved light-harvesting activity. The enhanced light-harvesting intensity of the CdG1, CdG2, and CdG3 composites could become a type of visible light driven photocatalyst.

The diffuse reflectance spectra of $CdLa_2S_4$ and $CdLa_2S_4$/rGO were transformed by performing the Kubelka-Munk transformation of the measured reflectance according to the following equation.

$$K=(1-R)^2/2R=F(R) \quad ①$$

K is the reflectance transformed according to Kubelka-Munk, R is the reflectance (%), and F(R) is the so-called remission or Kubelka-Munk function. It is well known that the band gap E_g and the absorption coefficient α are related, as shown in the following equation.

$$\alpha h\nu = A(h\nu - E_g)^{1/2} \quad ②$$

where α, ν, E_g, and A are the absorption coefficient, light frequency, band gap, and a constant, respectively. If the compound scatters in a perfectly diffuse manner, K becomes equal to 2α. In this case, we can use the following expression;

$$[F(R)h\nu]^2 = A(h\nu - E_g) \quad ③$$

The estimated Eg value was 2.1 eV for the $CdLa_2S_4$ sample. This value is red shifted from the typical Eg of the $CdLa_2S_4$/rGO, to obtain CdG3 (2.46 eV)> CdG2 (2.35 eV)> CdG1 (2.22 eV) of the PGT nanocomposites shown in Fig. 4b.

XPS was carried out for the qualitative analysis of the $CdLa_2S_4$/rGO (CdG2) nanocomposite containing $CdLa_2S_4$ and graphene. The XPS survey spectrum had peaks corresponding to Cd, La, S, O, and C consistent with the formation of the CdG2 nanocomposites shown in Fig. 5a. Fig. 5b shows the C1s spectra of the carbon presented in the composites. The C1s has a strong peak located at around 284.6 eV and a slight peak at 289.1 eV. These binding energies correspond to the C-O and C=O functional groups, respectively. These results reveal that our nanocomposites still contain some partial oxygen functional groups. The presence of oxygen functional groups may increase the light absorption towards the visible region.[40] Fig. 5c shows that the O1s photoelectron kinetic energies are smaller than those of the C1s, thus the sampling depth is smaller, and therefore the O1s spectra are slightly more surface specific. We assigned the O1s peak at 532.1 eV to contributions from the C=O and O-C–OH groups; this means that after the heat treatment, the conversion to other chemical species may be possible.[41-43] The remaining peak at 534.7eV indicates that the C–OH group is still appearing, it is assumed that the reduction of the remaining C–OH groups in reduced graphene oxide is very difficult or it may not be possible with our heat treated condition.[44] Fig. 5d shows the La3d peaks which are located at three different binding energy values. The binding energy positions located at 838.3 eV and 857.6eV were ascribed to La3d $_{3/2}$ and La3d $_{5/2}$, respectively, which are consistent with the binding energy of La^{3+} .[21] The S species were mainly present in −2 states, corresponding to the HS-groups with the binding energy at around 163.5 in the S2p level.[45] The binding energy value of S2p $_{3/2}$ is 161.2 eV and that of S2p $_{1/2}$ is 163.2 eV. The Cd 3d spectrum shown in Fig. 5f has a doublet feature due to the spin orbit splitting, whereby the 3d $_{5/2}$ and 3d $_{3/2}$ peaks agree with those reported in the literature.[46] The Cd 3d core level could be satisfactorily fit to a single spin-orbit pair at 405 eV (Cd3d $_{5/2}$) and at 412 eV (Cd3d $_{3/2}$).

The nitrogen adsorption isotherms of $CdLa_2S_4$, CdG1, CdG2, CdG3 composites and pore-size distribution curves of CdG2 are shown in Fig. 6. The formation of type II adsorption isotherms confirmed the major presence of micropores and the minor presence of mesopores

on the surfaces of the $CdLa_2S_4$ and the CdG1, CdG2, and CdG3 composites. This indicates that the $CdLa_2S_4$/rGO composites studied were mainly micro- and mesoporous in character, with a minor presence of wider pores where capillary condensation occurred. The type II isotherms do not exhibit a saturation limit, unlike type I. This type of isotherm indicates indefinite multi-layer formation after the completion of the monolayer, and is found in adsorbents with a wide range of pore sizes. All the isotherm shapes are similar for all $CdLa_2S_4$ series of as-prepared samples. Table 1 compares the textural properties of the as-prepared samples and their micro-structures. The surface areas and pore volumes of the $CdLa_2S_4$/rGO changed due to the chemical precipitation of the $CdLa_2S_4$ compounds via microwave assisted synthesis for 5 min; this indicated that the synthesis condition could be suitable to prepare nanomaterials with micropores and mesopores. The pore size distributions for the CdG2 sample are shown in the inset image of Table 1. The sample demonstrated the presence of a large number of pores in the broad pore distribution range of 0.7–0.9 nm.

Adsorption and photodecolorization process

To evaluate the adsorption ability of the as-prepared composite catalysts, the reactor was placed on the magnetic churn dasher, stirred for 120 min in a dark box to establish an adsorption–desorption equilibrium. As shown in Fig. 7a, the level of Rh.B adsorption by $CdLa_2S_4$/rGO was higher than that of the $CdLa_2S_4$ powder. The BET surface area of the $CdLa_2S_4$ control sample, and the as-prepared CdG1, CdG2, and CdG3 nanocomposites was 17.92 m^2/g, 43.08 m^2/g, 57.74 m^2/g, and 26.44 m^2/g, respectively. CdG2 exhibits the best adsorption effect for the Rh.B dye solution. After establishing an adsorption–desorption equilibrium for the CdG2 and CdG1 catalysts, 41.4% and 28.5% of the Rh.B dye solution was removed, respectively, while only 11% of the Rh.B solution is removed for pure $CdLa_2S_4$.

The effects of visible light irradiation on RhB degradation due to the pure $CdLa_2S_4$ and $CdLa_2S_4$/rGO (CdG1, CdG2, CdG3) composite catalysts were investigated. From Fig. 7b, we can find that after visible light irradiation for 150 min, the degradation effect of CdG2 is superior (87%), while the degradation ratio of CdG3 and CdG1 for the Rh. B solution is 48% and 50%, respectively. The overall catalytic efficiency is in the order of $CdLa_2S_4$< CdG3< CdG1< CdG2 nanocomposites, which demonstrate all $CdLa_2S_4$/rGO nanocomposites possess improved visible-light photocatalytic ativity than that of pure $CdLa_2S_4$. In addition, it also

reveals that the photocatalytic activity of the as-prepared $CdLa_2S_4$/rGO nanocomposites do not improve monotonously with increase of S^{2-} concentration. It can be seen that when the concentration of S^{2-} is less than 0.75mM, the photocatalytic activity is improved steadily with increasing amount of S precursor. However, further increase in concentration of S^{2-} (> 0.75mM) results in decreasing photocatalytic activity. Thus, it indicated that CdG2 catalyst exhibit the highest synergetic effect between $CdLa_2S_4$ and graphene sheet. All calculated -$\ln(C_t/C_{ads})$ values (with the restriction of C_{ads} being the initial concentration in the bulk solution after dark adsorption and t being the reaction time) were approximately linear with the irradiation time represented in Fig. 7c and summarized in Table 1. The Rh.B degradation rate constant for the CdG2 composites reached 1.27×10^{-2} min^{-1} under visible light irradiation.

Fig. 8 shows the UV-vis spectra of DPCO extract liquors in the presence of CdG1, CdG2, and CdG3 composites under visible light irradiation. 1,5-diphenyl carbazide (DPCI) can be oxidized by oxidizing substances into 1,5-diphenyl carbazone (DPCO). Under visible light irradiation, some electrons are transited from the valence band (VB) to the conduction band (CB). Simultaneously, the electron–hole pairs form on the surface or inside the CdG2 samples. The electrons and holes react with the molecular oxygen (O_2) dissolved in the aqueous solution and the water molecules (H_2O) absorbed on the surface of $CdLa_2S_4$/rGO, respectively, producing the super oxygen radical anions ($\bullet O_2^-$) and hydroxyl radicals (•OH). These obtained •OH can oxidize 1,5-diphenyl carbazide (DPCI) into 1,5-diphenyl carbazone (DPCO). The DPCO can be extracted using a benzene solvent and shows an absorbance at 560 nm wavelength. Sequentially, the production and output of •OH can be easily detected. According to the different irradiation times, the DPCO solution exhibits different absorbances and shows an obvious increase compared with the corresponding DPCO solution without any irradiation.[43] The above results suggest that the CdG2 composites are much more efficient than any other composites.

To better understand the formation mechanism and evolution of the hollow nanostructures, time-dependent experiments of the synthesized CdG2 nanocomposite were carried out. Deng et al. reported the formation mechanism of hollow nanostructures using a gas bubble as a soft template.[47] Based on this study, a plausible mechanism was proposed to address the template-free formation of hollow $CdLa_2S_4$ nanospheres (Fig. 9). This is because

microwave heating is rapidly delivered to the surface of the material by radiant and/or convection heating, which is transferred to the bulk of the material via conduction. During the heating process, the mechanism of the gas bubble formation can be followed:

$NH_3 \cdot H_2O$ < -- > $NH_3\uparrow + H_2O$ (1)

$S_2O_3^{2-} = SO_2 + S\downarrow + H_2O$ (2)

As shown in Fig. 9a (step a), the NH_3 bubble initially generated from the decomposition of $NH_3 \cdot H_2O$ not only inhibited particle agglomeration but also provided a soft gas template for the formation of the hollow nanosphere.[48] As the reaction time increased, the unstable $S_2O_3^{2-}$ easily decomposed to generate S and SO_2 gas, thus continuously promoting the formation of a hollow nanosphere.[49] HRTEM images of the as-prepared $CdLa_2S_4$ nanostructure immobilizing on the reduced graphene oxide (CdG2) at different reaction times (3min, 5min, and 7min, labeled as CdG2-3, CdG2-5, and CdG2-7, respectively) are shown in Fig. 9b. In our work, during the initial stage of the reaction, smaller $CdLa_2S_4$ nanoparticles aggregated together to form solid nanospheres with a loose structure. With prolonged microwave assisted hydrothermal treatment, the inner crystallites of the aggregates underwent mass transfer to the outer shell by a dissolution–recrystallization process at the cost of the small crystallites, which have higher surface energies and solubility than the larger crystallites. With the increasing reaction time, the outward migration of the $CdLa_2S_4$ crystal would result in the continued expansion of the interior space; thus, the inner space of the spheres is further increased, which results in the $CdLa_2S_4$ hollow structures. Furthermore, the effect of temperature on the $CdLa_2S_4$ morphology also supports the fact that Ostwald ripening effect is the essential mechanism.[50] Meanwhile, reproducibility study was performed as irradiating the solution by microwave under same condition for 3 times, the results were shown in Fig. 9c which conforms the reliability of synthesis nanospheres $CdLa_2S_4$ by domestic microwave.

The relationship between visible light photocatalytic TBA degradation and hollow nanostructured CdG2 nanocomposite (microwave treatment time 3min, 5min, and 7min labeled as CdG2-3, CdG2-5, and CdG2-7, respectively) was conducted. The λ_{max} values of TBA were found to be 275 nm, which are shown in Fig. 10a. It can be seen that the decolorization of TBA with high concentration is conspicuous in the presenceof sample CdG2. From Fig. 10b, it was obvious that the heat teatment time can remarkably influence the

presence of $CdLa_2S_4$ hollow nanospheres, which possess enhanced photocatalytic degradation effect of CdG2-7 is superior (86%), while the degradation ratio of CdG2-3 and CdG2-5 for the TBA solution is 58% and 74%, respectively. The results also imply that microwave irradiation plays a vital role, possibly related to crystallinity and structure distribution.[51]

To demonstrate the stability of the cyclic performance of the CdG2-7 photocatalyst, consecutive photocatalytic TBA degradation reactions were conducted under visible light irradiation. As shown in Fig. 10c, CdG2-7 did not exhibit any significant loss of photocatalytic activity after four runs of TBA degradation. These results indicate that the CdG2 photocatalyst has high stability, which can be attributed to the strong interactions between $CdLa_2S_4$ and rGO,[52] graphene modification improves not only the photocatalytic performance but also the long-term stability of $CdLa_2S_4$ nanocrystals while pure $CdLa_2S_4$ is usually stable in the photocatalytic process.[19-21] The XRD pattern of CdG2-7 after four recycling experiments was almost identical to that of the as-prepared sample (Fig. 10d).[53,54] This result is significant from a practical viewpoint, as the enhanced photocatalytic activity and stability will lead to a more cost-effective operation. These results further confirm that $CdLa_2S_4$/rGO nanocomposite can be used as a catalytic material in an environmental purification process or in waste water treatment in the future.

The scheme of charge transfer process between $CdLa_2S_4$ and graphene particles is shown in Fig. 11. When $CdLa_2S_4$ was illuminated with visible light, the semiconductor produced electrons (e^-) and holes (h^+) that gained enough energy or momentum to jump the forbidden gap or energy barrier denoted as (E_g). The electrons (e^-) traveled from the valence band (VB) to the conduction band (CB) of $CdLa_2S_4$, producing an increased number of electrons (e^-) and holes (h^+) pairs. Meanwhile, the graphene attached to the semiconductor material ($CdLa_2S_4$) assisted in the smooth transistion of transferring the electrons (e^-) to the CB of $CdLa_2S_4$, thereby increasing the number of electrons as well as the rate of electron-induced redox reactions. Based on the above discussion, the addition of graphene in the $CdLa_2S_4$ nanocomposite not only improved the visible light absorption intensity but also enhanced the photocatalytic activity of the nanocomposites because of the high charge seperation induced by the synergistic effects of graphene on $CdLa_2S_4$. The generated electrons (e^-) react with the dissolved oxygen molecules and produce oxygen peroxide radicals $O_2^{\bullet -}$. The positive charge

hole (h^+) can react with OH^- derived from H_2O to form hydroxyl radicals $OH\bullet$.[55] The Rh.B and TBA molecules can then be photocataytically degraded by oxygen peroxide radicals $O_2\bullet^-$ and hydroxyl radicals $OH\bullet$ to CO_2, H_2O, and other mineralization products. The reactions involved in the charge mobility and mineralization of the dyes are as follows:

$$CdLa_2S_4/rGO + \text{Visible light } (h\upsilon) \rightarrow CdLa_2S_4/rGO^+ + h^+ + e^- \quad (1)$$

$$H_2O \rightarrow H^+ + OH^- \quad (2)$$

$$h^+ + OH^- \rightarrow OH\bullet \quad (3)$$

$$O_2 + e^- \rightarrow O_2\bullet^- \quad (4)$$

$$Rh.B/TBA + OH\bullet + O_2\bullet^- \rightarrow CO_2 + H_2O + \text{mineralized by products} \quad (5)$$

Conclusions

In summary, a hollow sphere $CdLa_2S_4$/rGO nanocomposite was prepared vis a fast and facile microwave-assisted synthesis method in a domestic microwave oven. The $CdLa_2S_4$ triggered by precipitation reaction uniformly distributed on the graphene nanosheets with hollow sphere within 7 mins was observed. The strong interaction between $CdLa_2S_4$ and rGO makes the hollow sphere $CdLa_2S_4$/rGO nanocomposite with an optimum concentration of S^{2-}(0.75mM) to show highly enhanced and stable visible light photocatalytic activity for degradation of organic and industrial dyes. This work demonstrates the important role played by microwave in the preparations of rGO-based hollow sphere materials and provides new insights into the photocatalytic degradation of pollutants under visible light irradiation.

References

1 Q.Z. Wu, X. Chen, P. Zhang, Y.C. Han, X.M. Chen, Y.H. Yan, Cryst. Growth. Des. 8 (2008) 3010–3018.

2 J.Yang, J. Lee, J. Kang, K. Lee, J. Suh, H. Yoon, Langmuir. 24 (2008) 3417–3421.

3 A.B. Bourlinos, D. Petridis, M.A. Karakassides, Chem. Commun. 16 (2001) 1518–1519.

4 S.H. Im, U. Jeong, Y. Xia, Nat. Mater. 4 (2005) 671–675.

5 X.L. Yu, C.B. Cao, H.S. Zhu, Q.S. Li, C.L. Liu, Q.H. Gong, Adv. Funct. Mater. 17 (2007) 1397–1401.

6 J.G. Wang, F. Li, H.J. Zhou, P.C. Sun, D.T. Ding, T.H. Chen, Chem. Mater. 21 (2009) 612–620.

7 A. Wolosiuk, O. Armagan, P. V. Braun, J. Am. Chem. Soc. 127 (2005) 16356–163577.

8 P.V. Braun, P. Osenar, M. Twardowski, G.N. Tew, S.I. Stupp, Adv. Funct. Mater. 15 (2005) 1745–1750.

9 Y.W. Zhang, M. Jiang, J.X. Zhao, Z.X. Wang, H.J. Dou, D.Y. Chen, Langmuir. 21 (2005) 1531–1538.

10 X.W. Lou, L.A. Archer, Z.C. Chao, Adv. Mater. 20 (2008) 3987–4019.

11 Y.R. Ma, L.M. Qi, J. Colloid. Interface. Sci. 335 (2009) 1–10.

12 G.R. Li, D.L. Qu, X.L. Yu, Y.X. Tong, Langmuir. 24 (2008) 4254–4259.

13 L. Zhu, W.C. Oh, J. Multifunct. Mater. Photosci. 5 (2014) 153-170.

14 K.J. Huang, J.Z. Zhang, Y. Liu, Y.M. Liu, Int. J. Hydrogen. Energ. 40 (2015) 10158-10167.

15 Q. Mi, D.Q. Chen, J.C. Hu, Z.X. Huang, J.L. Li, Chin. J. Catal. 34 (2013) 2138-2145.

16 X.W. Ou, G. Lin, Z.T. Luo, J. Mater. Chem. A 2 (2014) 19214-19220.

17 W. J. Lou, M. Chen, X.B. Wang, W.M. Liu, Chem. Mater. 19 (2007) 872 – 878.

18 X. Cao, L. Gu, L. Zhuge, W. Gao, W. Wang, S. Wu, Adv. Funct. Mater. 16 (2006) 896 – 902.

19 B.B. Kale, J.O. Baeg, K.J. Kong, S.J. Moon, L.K. Nikam, K.R. Patil, J. Mater. Chem. 21 (2011) 2624–2631.

20 Y P. Yuan, S.W. Cao, L.S. Yin, L. Xu, C. Xue, Int. J. Hydrogen. Energy. 38 (2013) 7218–7223.

21 J.G. Hou, C. Yang, Z. Wang, S.Q. Jiao, H.M. Zhu, RSC Adv. 2 (2012) 10330-10336.

22 K. Ullah, S. Ye, L. Zhu, Z.D. Meng, S. Sarkar, W.C. Oh, Mater. Sci. Eng. B 180 (2014) 20-26.

23 S. Das, A. K. Mukhopadhyay, S. Datta and D. Basu, Bull. Mater. Sci. 32 (2009) 1-13.

24 L.K. Pan, X.J. Liu, Z. Sun, C.Q. Sun, J. Mater. Chem. A 1 (2013) 8299-8326

25 L. Zhu, S.B. Jo, S. Ye, K. Ullah, Z.D. Meng, W.C. Oh, J. Ind. Eng. Chem. 22 (2015) 264–271.

26 L. Zhu, G. Trisha, C.Y. Park, Z.D. Meng, W.C. Oh, Chin. J. Catal. 33 (2012) 1276-1283.

27 D. Li, M.B. Muller, S. Gilje, R.B. Kaner, G.G. Wallace, Nature. Nanotech. 3 (2008) 101-105.

28 W.C. Oh, M L. Chen, K. Zhang, F.J. Zhang, W.K. Jang, J. Korean Phys. Soc. 56 (2010) 1097-1102.

29 K. Ullah, Z.D. Meng, S. Ye, L. Zhu, W.C. Oh, J. Ind. Eng. Chem. 20 (2014) 1035-1042.

30 Y.Q. Zhan, F.B. Meng, Y.J. Lei, R. Zhao, J.C. Zhong, X.B. Liu, Mater. Lett. 65 (2011) 1737–1740.

31 M.S. Dresselhaus, A. Jorio, M. Hofmann, G. Dresselhaus, R. Saito, Nano. Lett. 10 (2010) 751-758.

32 W.X. Zhang, J.C. Cui, C.A. Tao, Y.G. Wu, Z.P. Li, L. Ma, Y.Q. Wen, G.T. Li, Angew. Chem. Int. Ed. 48 (2009) 5864-5868.

33 J. Lu, J.X. Yang, J. Wang, A. Lim, S. Wang, K.P. Loh, ACS Nano. 3 (2009) 2367-2375.

34 A.C. Ferrari, J.C. Meyer, V. Scardaci, C. Casiraghi, M. Lazzeri, F. Mauri, S. Piscanec, D. Jiang, K.S. Novoselov, S. Roth, A.K. Geim, Phys. Rev. Lett. 97 (2006) 187401–187404.

35 J. Wang, P.J. Yang, J.H. Zhao, Z.P. Zhu, Appl. Surf. Sci. 282 (2013) 930–936.

36 Y.L. Min, J.C. Fan, Q.J. Xu, S.Y. Zhang, J. Alloys. Compd. 609 (2014) 46–53.

37 H. Zhang, X.J. Lv, Y.M. Li, Y. Wang, J.H. Li, ACS Nano. 4 (2010) 380–386.

38 M. Niederberger, G. Garnweitner, F. Krumeich, R. Nesper, H. Colfen, M. Antonietti, Chem. Mater., 2004, 16, 1202-1208.

39 J. K. Lee, C. H. Jin, H.S. Kim, C.M. Lee, J. Korean. Phys. Soc., 2011, 58, 1279-1283.

40 K. Ullah, S. Ye, L. Zhu, S.B. Jo, W.K. Jang, K.Y. Cho, W.C. Oh, Solid. State. Sci. 31 (2014) 91-98.

41 T. Szabo, O. Berkesi, P. Forgó, K. Josepovits, Y. Sanakis, D.I. Petridis, I. Dékány, Chem. Mater. 18 (2006) 2740-2749.

42 H.K. Jeong, H.J. Noh, J.Y. Kim, M.H. Jin, C.Y. Park, Y.H. Lee, EPL. 82 (2008) 67004–67005.

43 D.R. Dreyer, S.J. Park, C.W. Bielawski, R.S. Ruoff, Chem. Soc. Rev. 39 (2010) 228–240.

44 W. Gao, L.B. Alemany, L. Ci, P.M. Ajayan, Nature. Chem. 1 (2009) 403-408.

45 J.L. Huang, D.G. Gray, C.J. Li, J. Org. Chem. 9 (2013) 1388–1396.

46 G. Hota, S.B. Idage, K.C. Khilar, Colloid. Surface. A 293 (2007) 5–12.

47 Q. Peng, Y.J. Dong, Y.D. Li, Angew. Chem. Int. Ed. 42 (2003) 3027–3030.

48 X.Y. Chen, Z.H. Wang, X. Wang, R. Zhang, X.Y. Liu, W.J. Lin, Y.T. Qian, J. Crystal. Growth. 263 (2004) 570-574.

49 L.L. Xie, R.Wu, J. Li, Y.F. Sun, J.K. Jian, Chinese. J. Inorg. Chem. 27 (2011) 95-99.

50 X.P. Li, Y.A. Gao, L. Yu, L.Q. Zheng, J. Solid. State. Chem. 183 (2010) 1423–1432.

51 Y. Liu, Y. Hu, M.J. Zhou, H.S. Qian, X. Hu, Appl. Catal. B. 125 (2012) 425-431.

52 P. Gao, J.C. Liu, D.D. Sun, W.J. Ng, J. Hazard. Mater. 250 (2013) 412-420.

53 H.G. Yu, L.L. Xu, P. Wang, X.F. Wang, J.G. Yu, Appl. Catal. B: Environ. 144 (2014) 75–82.

54 J.F. Guo, B. Ma, A. Yin, K. Fan, W.L. Dai, J. Hazard. Mater. 212 (2012) 77–82.

55 Z.D. Meng, T. Ghosh, L. Zhu, J.G. Choi, C.Y. Park, W.C. Oh, J. Mater. Chem. 22 (2012) 16127-16135.

Table 1. BET surface areas, textural properties, and visible light photo-degradation rate (k_{app}) constants of as-prepared samples.

Sample	$CdLa_2S_4$	CdG1	CdG2	CdG3
BET surface area,m^2/g	17.92	43.08	57.74	26.44
Total pore volume,cm^3/g	0.048	0.085	0.095	0.049
Average pore diameter, nm	10.8	7.91	7.28	7.42
$k_{app}(min^{-1})$	1.28×10^{-3}	4.35×10^{-3}	1.27×10^{-2}	3.03×10^{-3}

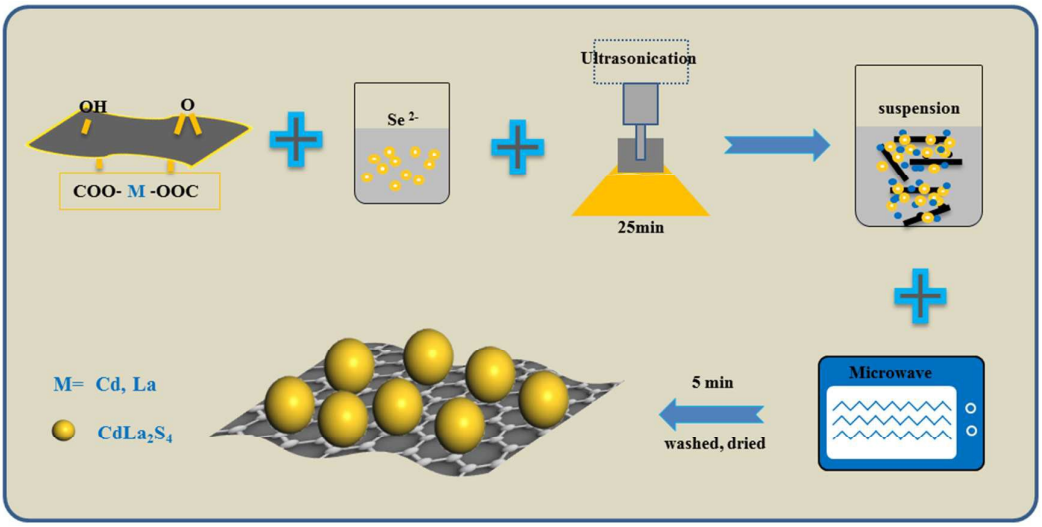

(a)

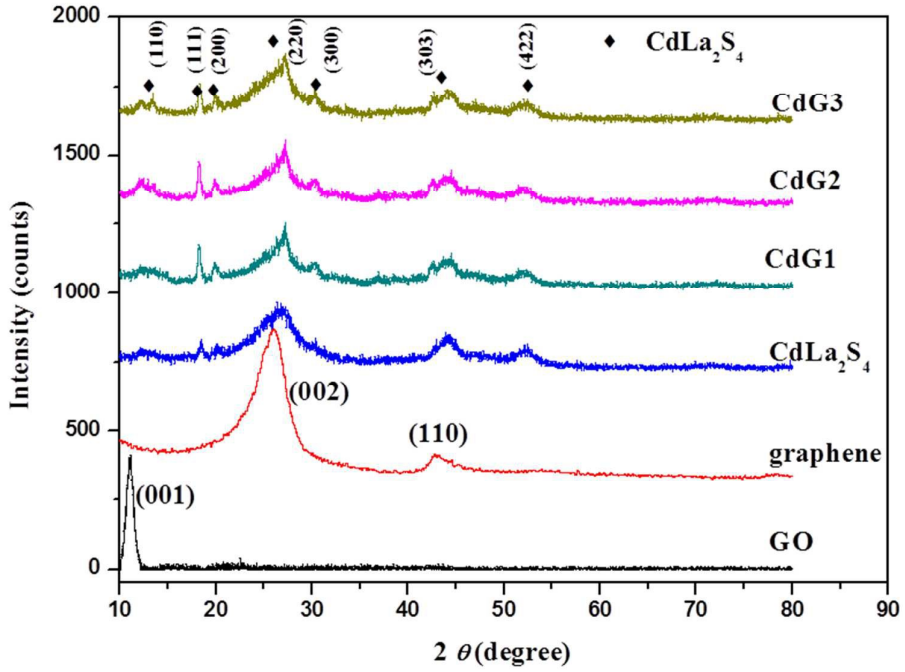

(b)

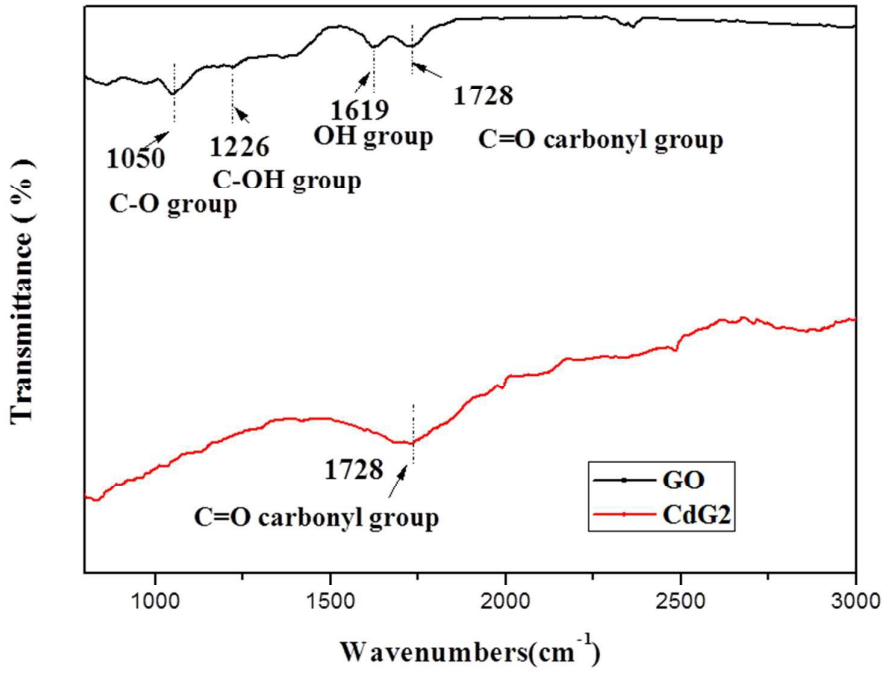

(c)

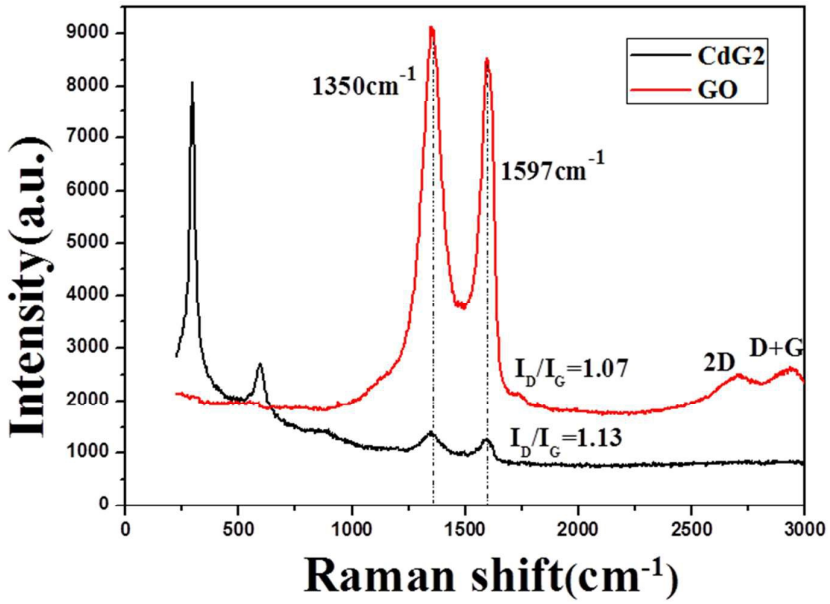

(d)

Fig. 1. (a) Schematic illustration of deposition of $CdLa_2S_4$ nanoparticles on the GONS, (b) XRD patterns of GO, graphene, $CdLa_2S_4$, CdG1, CdG2, and CdG3, (c) FT-IR spectra of GO and CdG2, (d) Raman shift of GO and CdG2.

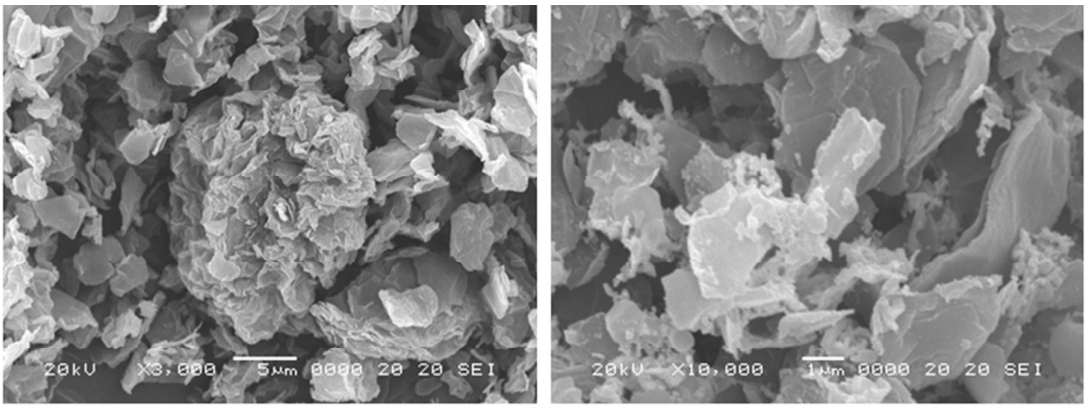

(a)

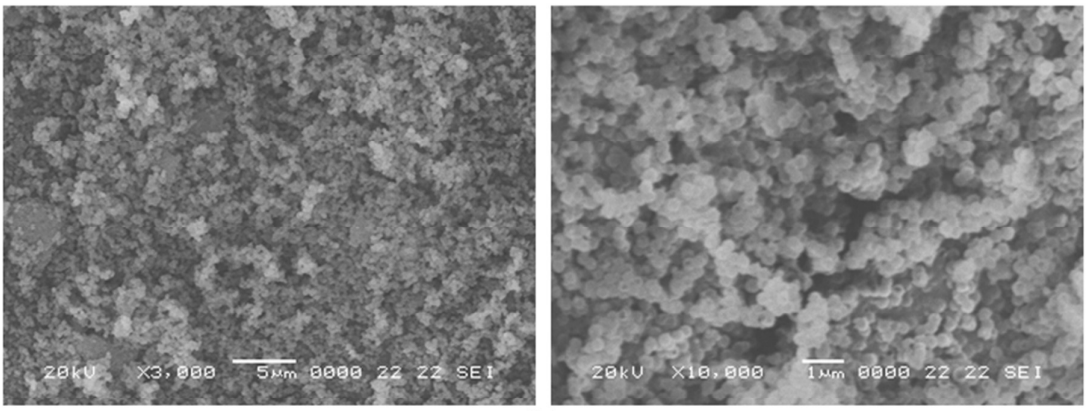

(b)

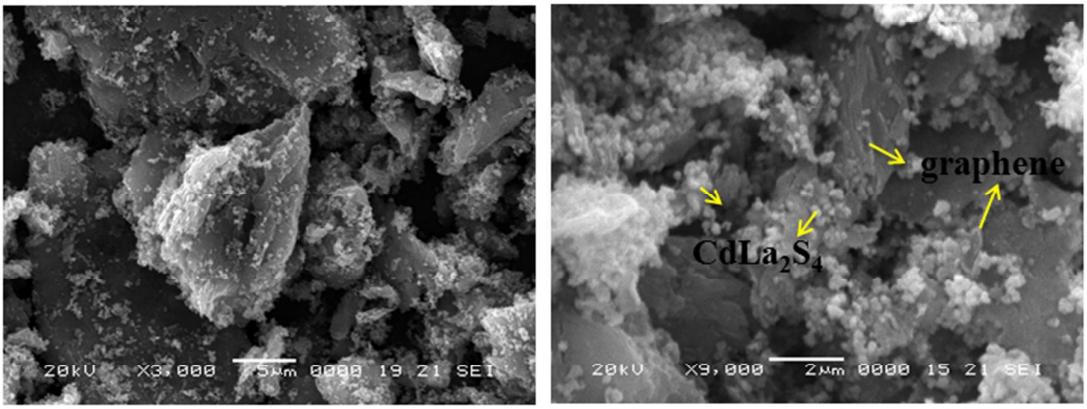

(c)

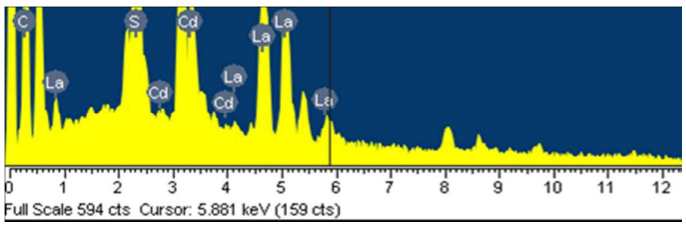

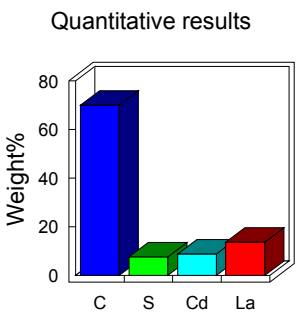

(d)

Fig. 2. SEM micrographs of as-prepared samples: (a) graphene, (b) $CdLa_2S_4$ nanoparticle, (c) CdG2 nanocomposite, (d) EDX elemental microanalysis and element weight % of CdG2 nanocomposite.

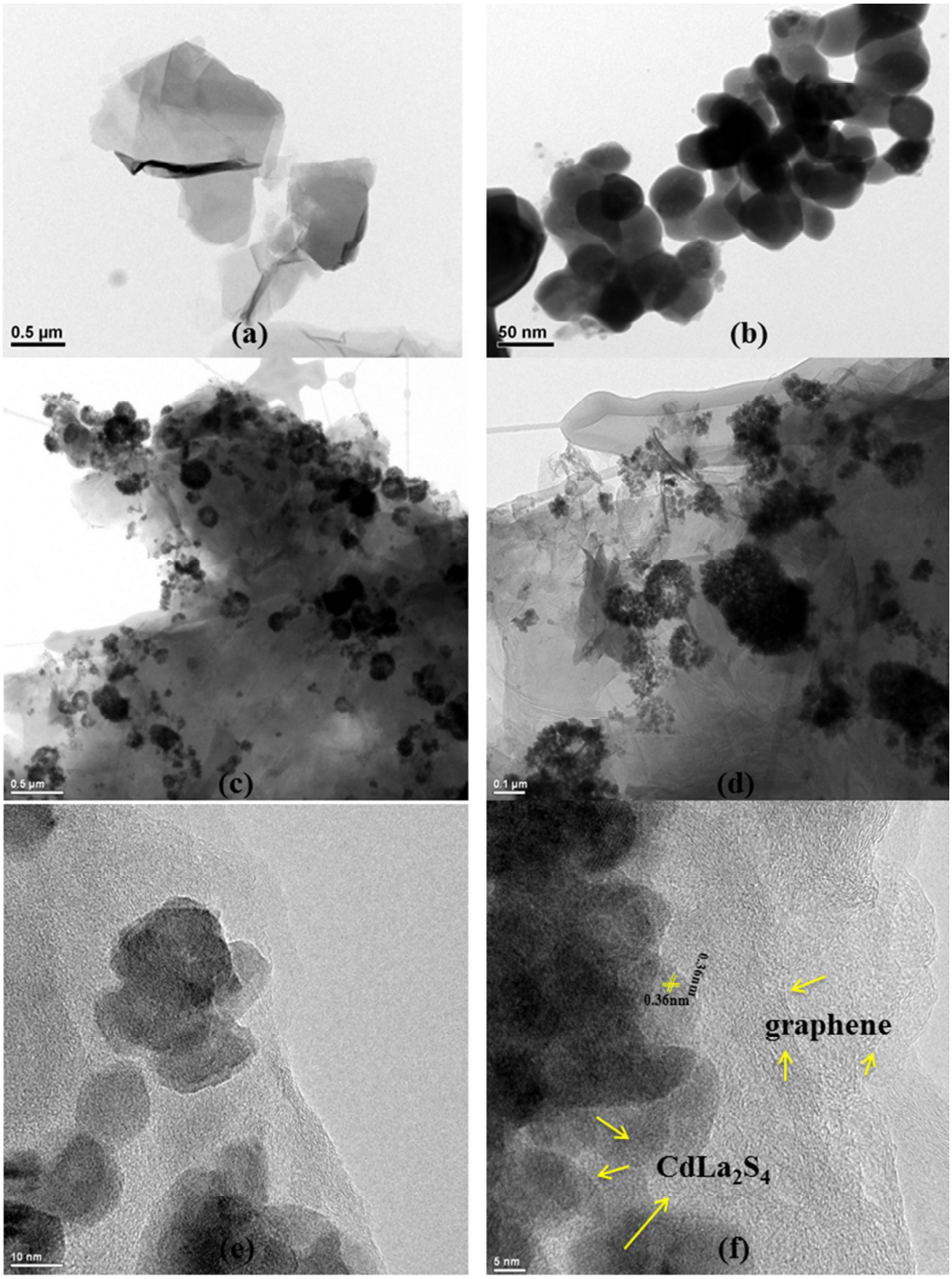

Fig. 3. TEM micrographs of as-prepared samples: (a) graphene, (b) $CdLa_2S_4$ nanoparticle, (c-f) TEM and HRTEM images of CdG2 nanocomposite.

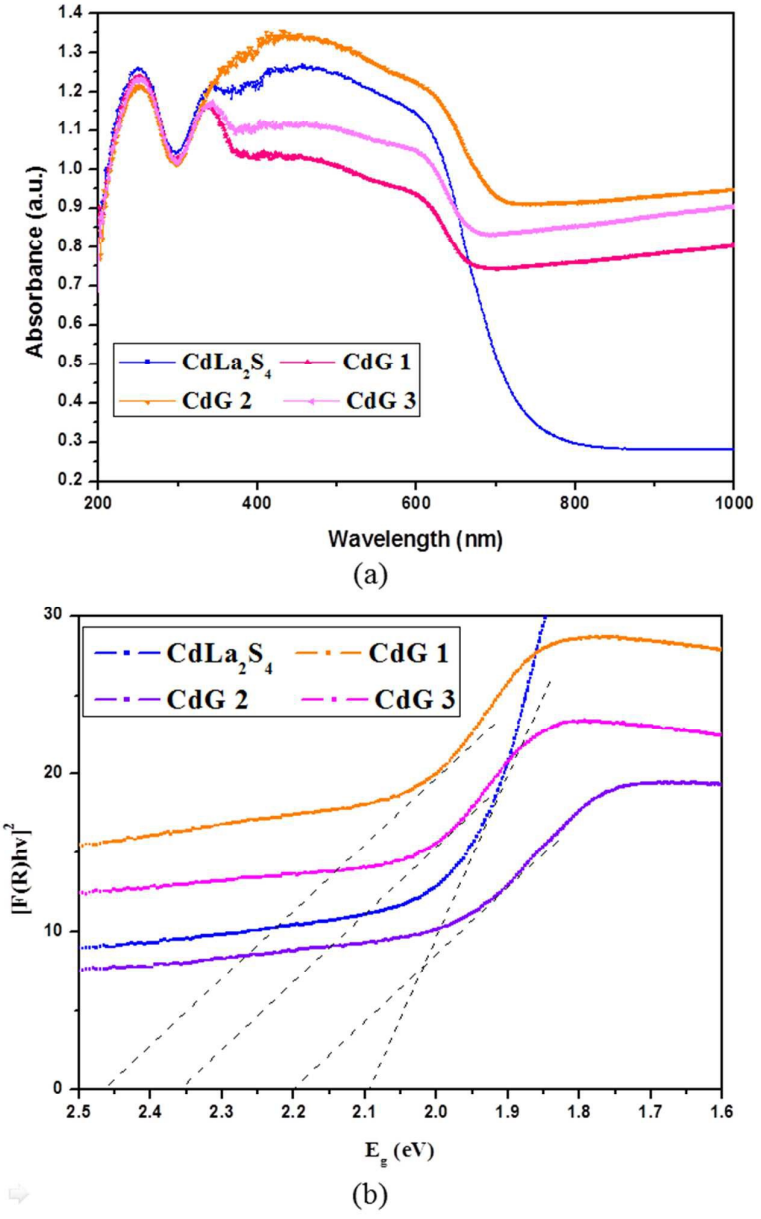

Fig. 4. (a) UV-vis absorbance spectra (b) Variation of $(\alpha hv)^2$ versus photon energy (hv) of $CdLa_2S_4$, CdG1, CdG2, and CdG3.

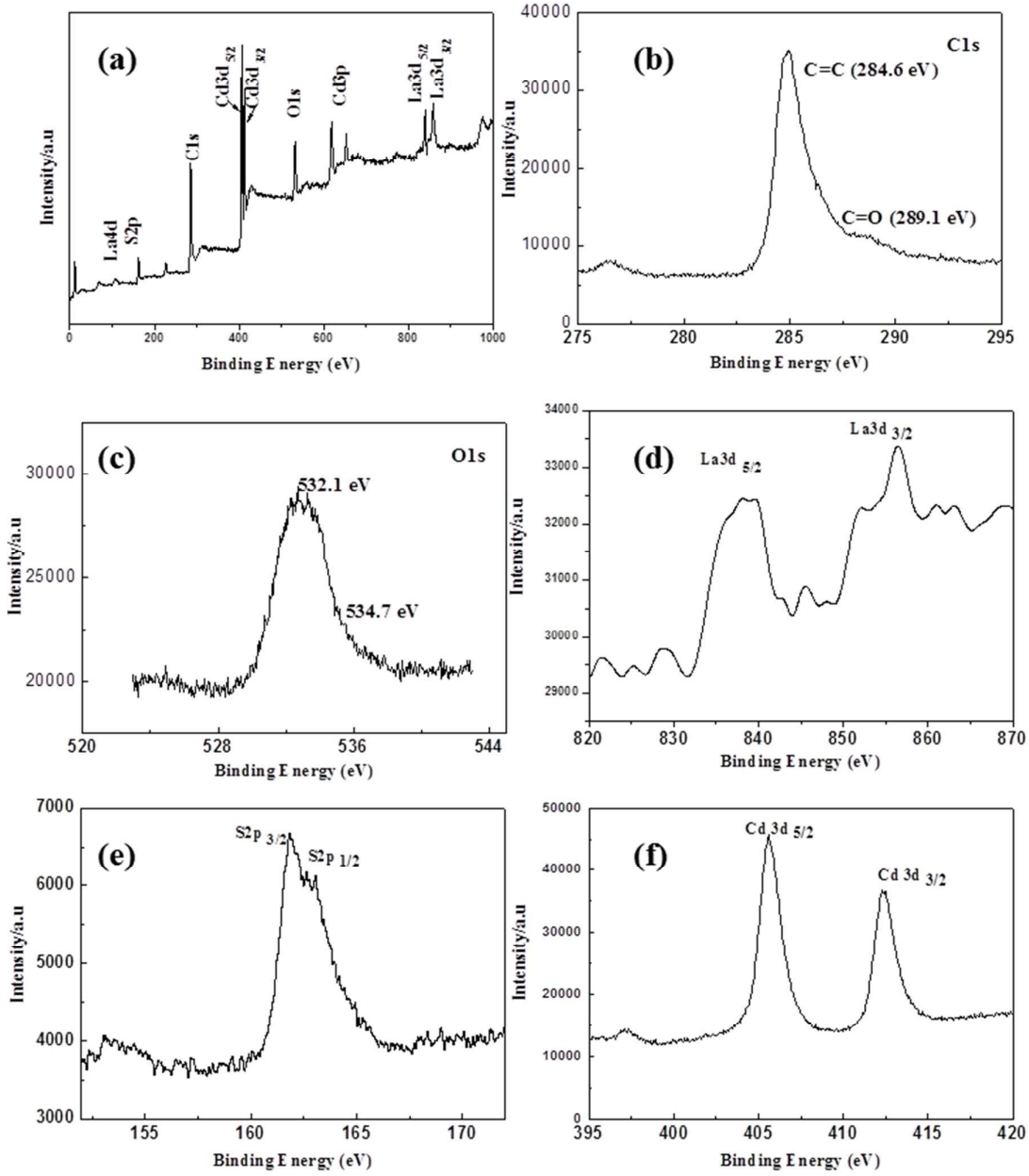

Fig. 5. XPS results of CdG2 nanocomposite photocatalyst (a) survey scan spectra, (b) C1s, (c) O1s, (d) La3d, (e) S2p, (f) Cd3d.

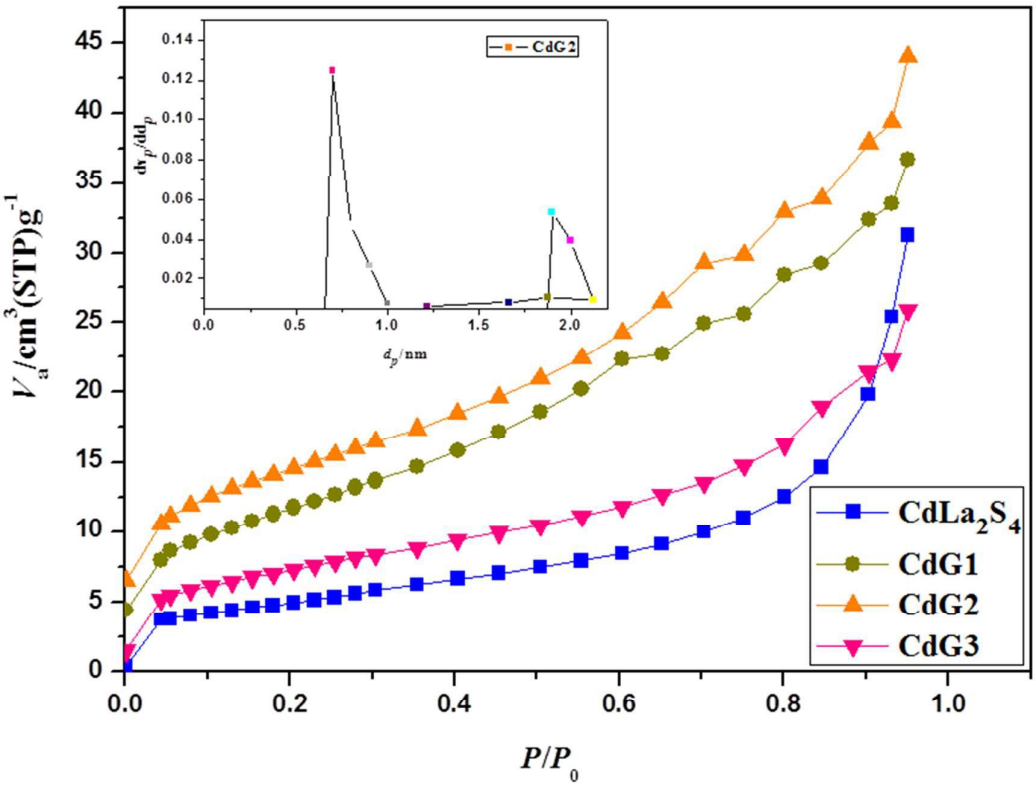

Fig. 6. N_2 adsorption isotherms of $CdLa_2S_4$, CdG1, CdG2, and CdG3, as well as BJH pore size distributions obtained from the CdG2 composite.

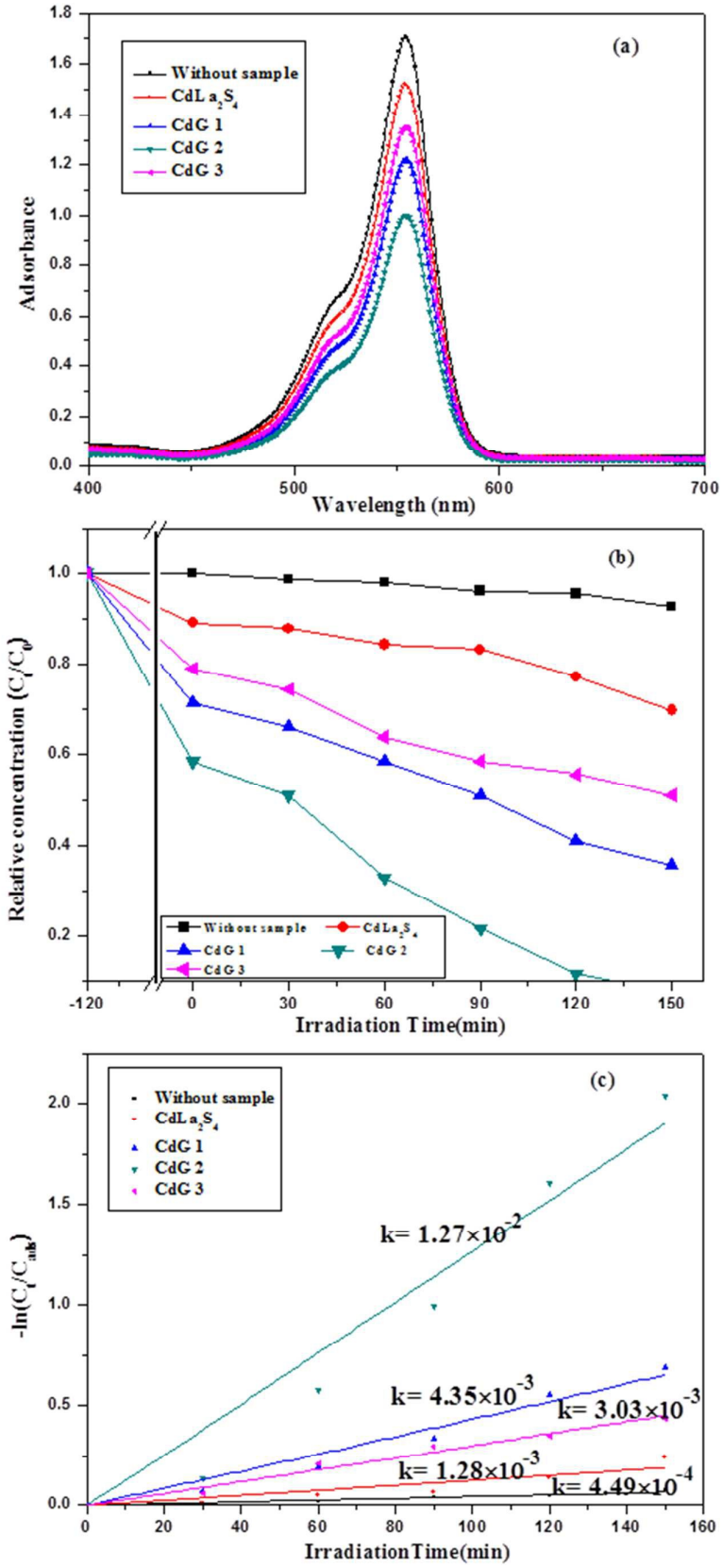

Fig. 7. (a) UV/Vis spectra of Rh.B concentration against the as-prepared samples after adsorption–desorption equilibrium. (b) Degradation of Rh.B dye (3×10^{-5} mol/L, 50 mL) with different samples (0.03g). (c) Apparent first order kinetics of Rh.B degradation over $CdLa_2S_4$, CdG1, CdG2, and CdG3 under visible light irradiation.

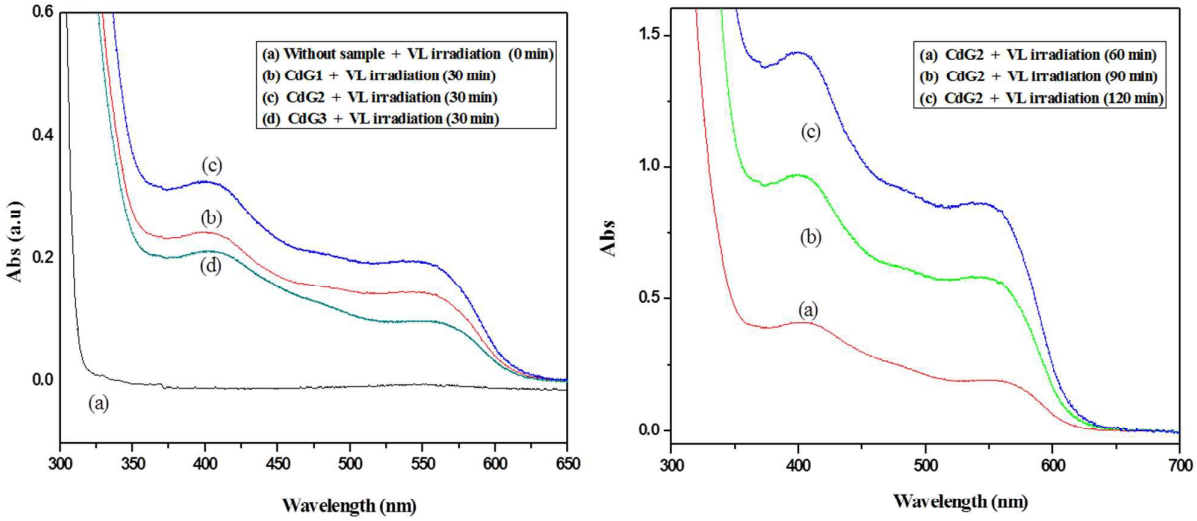

(a) (b)

Fig. 8. (a) UV-vis spectra of DPCO extract liquors in the presence of different samples under visible light irradiation for 30min. (b) UV-vis spectra of DPCO extract liquors in the presence of CdG2 for different irradiation times.

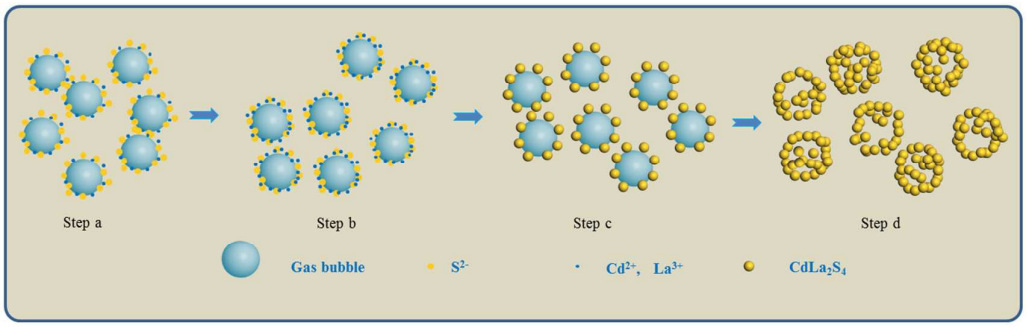

(a)

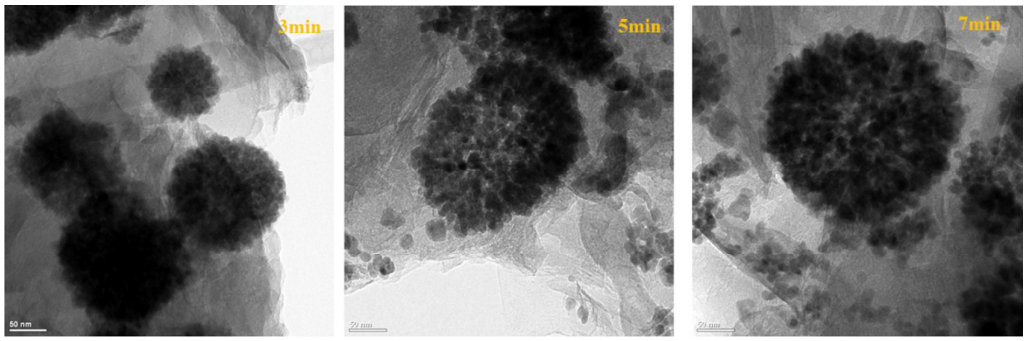

(b)

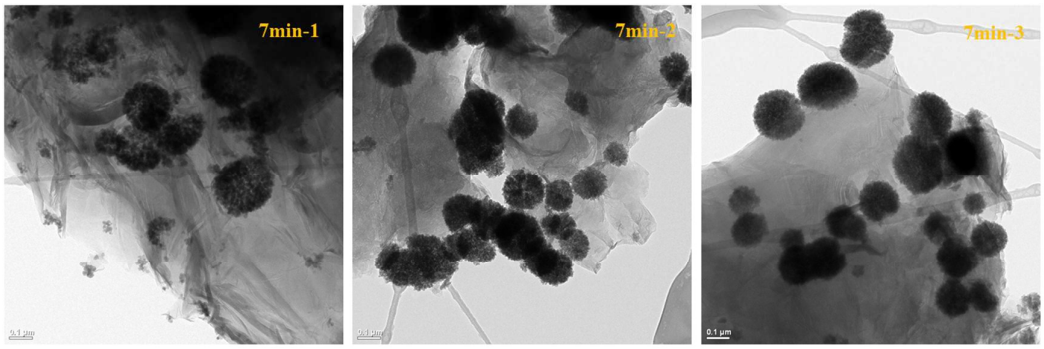

Fig. 9. (a) Schematic illustration of the formation of the $CdLa_2S_4$ (0.75mM) nanostructures. (b) HRTEM images of the as-prepared $CdLa_2S_4$ (0.75mM) nanostructure immobilizing on reduced graphene oxide at different reaction times (3min, 5min, and 7min). (c) Reproducibility study of synthesis $CdLa_2S_4$ by microwave at 7min for 3 times.

.

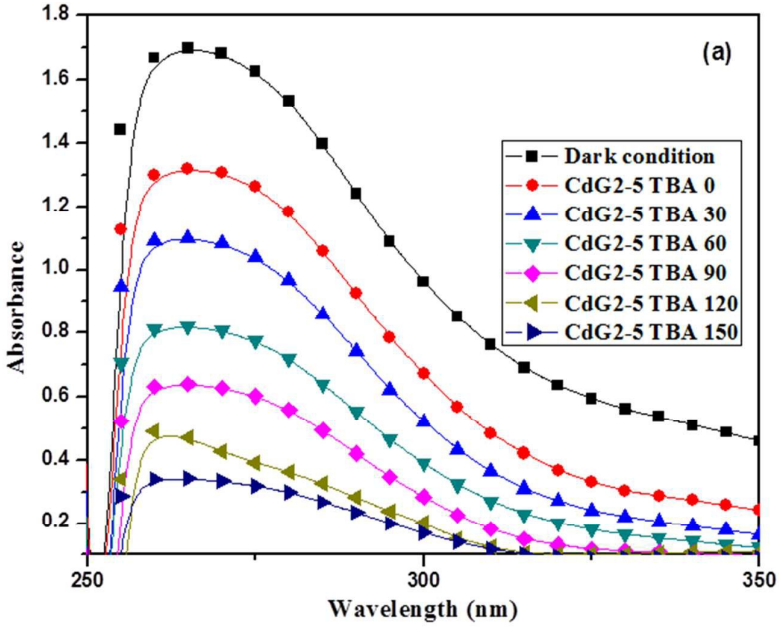

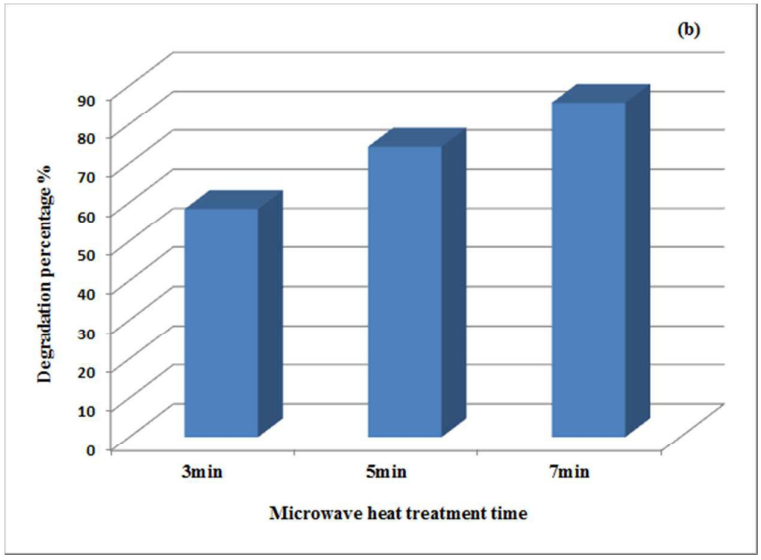

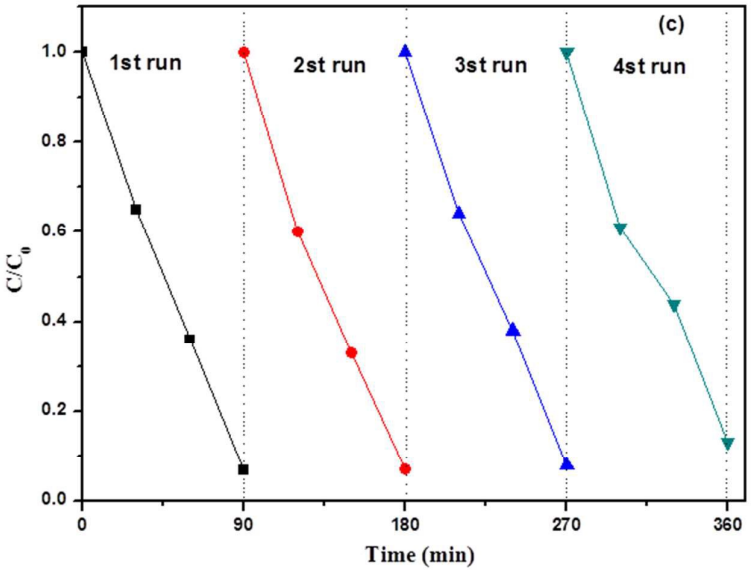

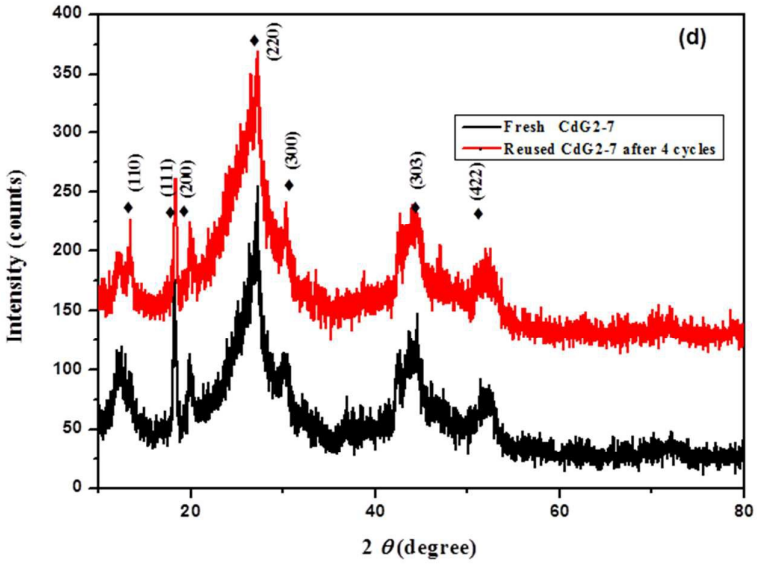

Fig. 10. (a) Temporal evolution of the UV/Vis spectra of TBA mediated by CdG2-5 nanocomposite under visible light irradiation (50 mL, 3.0×10^{-5} mol/L). (b) Photodegradation efficiencies of TBA over CdG2-3,5,7 prepared at different reaction times. (c) Cycling runs of the photocatalytic degradation of TBA with CdG2-7 nanocomposite under visible light irradiation.(d) XRD patterns of the fresh and the reused CdG2-7 nanocomposite after 4 cycles.

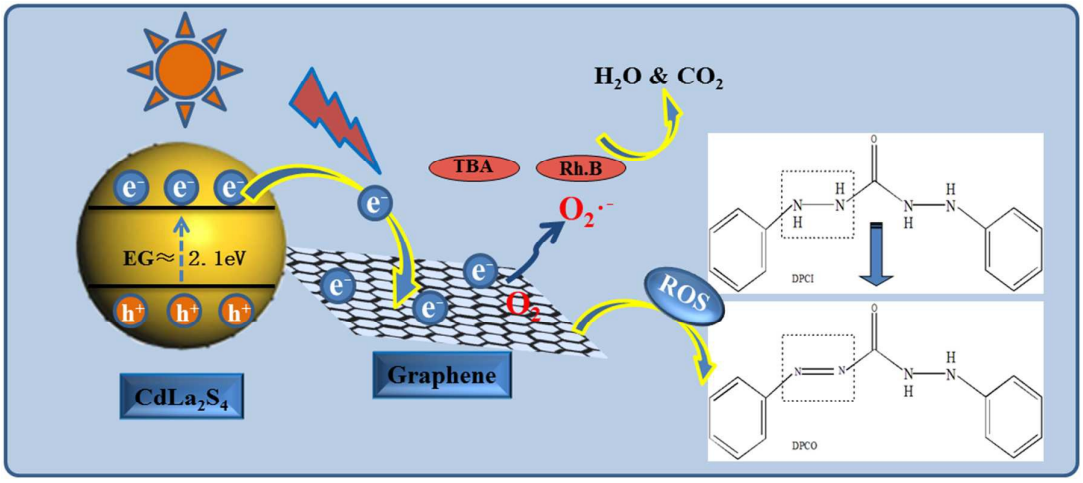

Fig. 11. Schematic drawing of photocatalytic degradation Rh.B, TBA dyes and ROS generation on the interface of $CdLa_2S_4$/rGO sample under visible light irradiation.